arXiv:1202.1894v1 [cond-mat.supr-con] 9 Feb 2012

A Triplet Superconductor UPt$_3$

Yasumasa Tsutsumi and Kazushige Machida
Department of Physics, Okayama University, Okayama 700-8530, Japan

Tetsuo Ohmi
Department of Physics, Kinki University, 3-4-1 Kowakae, Higashi-Osaka, 577-8502, Japan

Masa-aki Ozaki
Uji, 611-0002, Japan

(Dated: February 10, 2012)

Motivated by recent angle-resolved thermal conductivity experiment that shows twofold gap symmetry in the high field and low temperature C phase in a heavy fermion superconductor UPt$_3$, we group-theoretically identify the pairing functions as E_{1u} with the f-wave character for all three phases. Those are consistent with this observation in addition to variety of existing measurements. By using microscopic quasi-classical Eilenberger equation with this identified triplet pairing function under applied fields, we develop detailed studies of the vortex structures for three phases, including the vortex lattice symmetry, local density of states, and the internal field distribution. These quantities are directly measurable experimentally via SANS, STM/STS, and NMR, respectively. It is found that in the B phase of low H and low T the double-core vortex is stabilized over the singular vortex. For the C phase thermal conductivity data are analyzed to confirm the gap structure proposed. We also give detailed comparisons of various proposed pair functions, concluding that the present E_{1u} with f-wave, which is analogue to the triplet planar state, is better than E_{2u} or E_{1g} scenarios. Finally we touch upon the surface topological aspects of Majorana modes associated with the E^f_{1u} state of the planar like features.

I. INTRODUCTION

UPt$_3$[1] belongs to the first generation of the family of heavy fermion superconductors together with CeCu$_2$Si$_2$ and UBe$_{13}$ and has unique superconducting properties among them. Soon after the pioneering discovery[2] of the double superconducting transition, it is found[3–5] that the phase diagram in H vs T plane consists of three A, B and C phases. The A (C) phase is in high (low) temperature and low (high) field while the B phase is in the low T and low H. It is rather obvious to recognize that the order parameter (OP) must be multi-components. The main argument is centered on how to understand this phase diagram, or on what OP can describe it in a consistent manner[6,7]. Now the splitting of the superconducting transition temperatures $T_{c1} \cong 550$ mK and $T_{c2} \cong 500$ mK is generally understood due to a symmetry breaking field for otherwise doubly degenerate pairing state. The identification of this symmetry breaking field is still not settled yet, but it is considered as coming from the antiferromagnetic (AF) ordering at $T_N = 5$ K[8–14] or coming from the crystal lattice symmetry lowering that occurs at a higher temperature[15].

The remaining question is to identify the OP symmetry. The central discussions are on what causes the OP degeneracy, either due to the orbital part[6,8,13,14] or the spin part of the OP[9–12]. The former scenario has a fundamental difficulty where the so-called gradient coupling term in the Ginzburg-Landau (GL) functional inevitably avoids the observed crossing of the two transition lines starting from T_{c1} and T_{c2}, removing the C phase. Therefore the orbital scenario needs a fine tuning of the underlying Fermi surface topology and the detailed structure of the orbital function[6,16]. Among various proposals the E_{2u} symmetry is regarded as a most possible candidate where $\boldsymbol{d}(\boldsymbol{k}) \propto \boldsymbol{z}(k_x^2 - k_y^2 + 2ik_xk_y)k_z$. This state is time reversal symmetry broken and fourfold symmetric in the A and C phases. In the B phase, there exist a line node in the equator and two point nodes in the poles.

On the other hand, the spin scenario[9–12,17–21] is free from this difficulty, but a difficulty to qualitatively estimate the spin-orbit (SO) coupling remains because the spin scenario assumes the weak SO coupling in contrast with the strong SO coupling assumption adopted in the E_{2u} scenario[6,13,14,16,22,23]. This controversy is resolved experimentally because the Knight shift[24,25] starts decreasing below T_{c2} when $H \sim 2$ kG for $H \parallel c$. This field $H_{\rm rot}$ corresponding to the rotation of the d-vector[25] gives an estimate of the SO coupling strength in this system, justifying the classification scheme from the weak SO coupling, which never attains in the strong SO case where the d-vector is strongly tied to the underlying crystalline axes via the orbital part in OP.

The basic requirements of the possible pairing state realized in UPt$_3$ can be summarized as follows: (1) The gap structure contains both horizontal line node(s) and point nodes as evidenced by power law behaviors in various directional dependent transport measurements, such as thermal conductivity[26,27], ultrasound attenuation experiments[28–31] and also bulk measurements, such as specific heat[3,32,33], penetration depth[34], nuclear relaxation time[35], and magnetization[36] experiments. (2) As mentioned, the detailed Knight shift experiment[25] shows the decrease of the magnetic susceptibility below T_{c2}, depending on the field direction and its strength. Then it is concluded that the d-vector contains the $\boldsymbol{b}$-component and $\boldsymbol{c}$-component in the B phase for the hexagonal crystal. Upon increasing H ($\parallel c$) this $\boldsymbol{c}$-component turns to be the $\boldsymbol{a}$-component. (3) Finally according to the recent angle-resolved thermal conductivity measurement[37] it is found that the twofold symmetric gap structure in the basal plane for the C phase, the full rotational symmetry in the B phase and the horizontal line nodes at the tropical position, not on the equator of the Fermi sphere.

In view of those previous[7] and recent experiments[37] we come to a new stage to critically examine the proposed pairing states belonging to the orbital scenario; the singlet category E_{1g}[38] and the triplet category E_{2u}[13,14] in addition to the so-called accidental degeneracy scenario[39,40] and also belonging to the spin scenario[9–12,17–21].

Previously we have tentatively chosen the orbital part from E_{1u} representation[17–20] where the OP is non-unitary and also from E_{2u} representation[21] in our spin scenario among the classified pairing functions in the absence[41,42] and in the presence of the antiferromagnetism[43]. However, the precise orbital form is still to be determined. In view of this finding we are now in the position to identify the precise pair functions for all A, B, and C phases, based on the spin degeneracy scenario.

The arrangement of the paper is as follows. We first classify the pairing function group-theoretically and examine the possible symmetry realized in connection with various existing experimental data in Sec. II. The formulation is given in Sec. III based on the quasi-classical Eilenberger theory. With the identified pair function we investigate the vortex structures in the B phase, including the exotic vortex core structure, namely the so-called double-core structure associated with multi-component OP in Sec. IV. The present study here is a natural extension of our GL framework for multiple OP[44–46] to microscopic calculation based on Eilenberger theory, that provides the quasiparticle (QP) structures in periodic vortex lattices. The vortex structure is also studied for the A and C phases in connection with the twofold gap function in Sec. V. The final section is devoted to conclusion and future perspectives where detailed comparisons with other proposed pairing functions are made. We use the two notations (x, y, z) and (a, b, c) to denote the spatial coordinates interchangeably.

II. CLASSIFICATION OF POSSIBLE PAIRING STATES

In this section we first enumerate possible pairing states group-theoretically[41,42,47]. The classified states are all so-called inert phase that is stable under a small change of the system parameters and differs from the previous classifications where we only treat the p-wave states[41,42]. By the same procedure as in refs. 41 and 42, we can easily extend it to the f-wave pairing states with the orbital angular momentum $l = 3$.

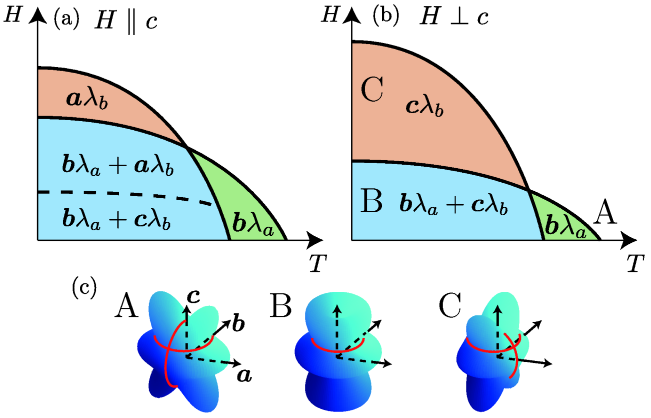
H
(a) $H \parallel c$
$\boldsymbol{a}\lambda_b$
$\boldsymbol{b}\lambda_a + \boldsymbol{a}\lambda_b$
$\boldsymbol{b}\lambda_a + \boldsymbol{c}\lambda_b$
$\boldsymbol{b}\lambda_a$
T
H
(b) $H \perp c$
C $\boldsymbol{c}\lambda_b$
B $\boldsymbol{b}\lambda_a + \boldsymbol{c}\lambda_b$
$\boldsymbol{b}\lambda_a$
A
T
(c)
A
c
b
a
B
C

FIG. 1. (Color online) Schematic phase diagrams under $H \parallel c$ (a) and $H \perp c$ (b). Orbital states are $\lambda_a(\boldsymbol{k}) = \sqrt{21/8}k_a(5k_c^2 - 1)$ and $\lambda_b(\boldsymbol{k}) = \sqrt{21/8}k_b(5k_c^2 - 1)$. (c) Gap functions of the three A, B, and C phases.

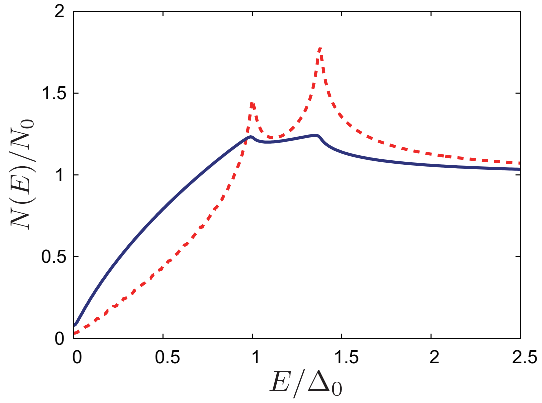

FIG. 2. (Color online) DOS in the bulk for A and C phases $|\Delta(\boldsymbol{k})| = \Delta_0|k_x(5k_z^2 - 1)|$ (solid line) and B phase $|\Delta(\boldsymbol{k})| = \Delta_0\sqrt{k_x^2 + k_y^2}|5k_z^2 - 1|$ (dashed line).

Table I lists all possible f-wave inert states and its little group under hexagonal symmetry D_6. Here the basis functions of the irreducible representations are also given in Table I. As mentioned before the required properties are all satisfied by the planar state $\hat{\tau}_x l_1^{E_{1u}} + \hat{\tau}_y l_2^{E_{1u}}$ in E_{1u}. Namely in terms of the present context of UPt$_3$, $(\boldsymbol{c}k_b + \boldsymbol{b}k_a)(5k_z^2 - 1)$ where the unit vectors $\boldsymbol{a}$, $\boldsymbol{b}$ and $\boldsymbol{c}$ in D_6 denote the d-vector component. Note that this state is a natural extension of the planar state $\hat{\tau}_x k_x + \hat{\tau}_y k_y$ in the p-wave state that is realized in thin films of the superfluid ^{3}He B-phase.

A. Phase assignment and gap structures

This E_{1u} state is assigned to each phase as the B phase $(\boldsymbol{c}k_b + \boldsymbol{b}k_a)(5k_c^2 - 1)$, the A phase $\boldsymbol{b}k_a(5k_c^2 - 1)$, and the C

TABLE I. f-wave inert phase and its little group in D_6 system.

rep.	state	order parameter	basis of irr. rep.	little group
A_{2u}	A_{2u}-polar	$\hat{\tau}_z l^{A_{2u}}$	$l^{A_{2u}}=2k_z^3-3(k_x^2+k_y^2)k_z$	$(1+C'_{21}u_{2x})(1+C'_{21}\tilde{\pi})\{\boldsymbol{C}_6\times\boldsymbol{A}(\boldsymbol{e}_z)\times T\}$
	A_{2u}-β	$(\hat{\tau}_x+i\hat{\tau}_y)l^{A_{2u}}$		$(1+tu_{2x})(1+C'_{21}u_{2z})\{\boldsymbol{C}_6\times\tilde{\boldsymbol{A}}(\boldsymbol{e}_z)\}$
B_{1u}	B_{1u}-polar	$\hat{\tau}_z l^{B_{1u}}$	$l^{B_{1u}}=k_x^3-3k_y^2k_x$	$(1+C_2u_{2x})(1+C''_{21}\tilde{\pi})\{\boldsymbol{D}'_3\times\boldsymbol{A}(\boldsymbol{e}_z)\times T\}$
	B_{1u}-β	$(\hat{\tau}_x+i\hat{\tau}_y)l^{B_{1u}}$		$(1+tu_{2x})(1+C_2u_{2z})\{\boldsymbol{D}'_3\times\tilde{\boldsymbol{A}}(\boldsymbol{e}_z)\}$
B_{2u}	B_{2u}-polar	$\hat{\tau}_z l^{B_{2u}}$	$l^{B_{2u}}=3k_yk_x^2-k_y^3$	$(1+C_2u_{2x})(1+C'_{21}\tilde{\pi})\{\boldsymbol{D}''_3\times\boldsymbol{A}(\boldsymbol{e}_z)\times T\}$
	B_{2u}-β	$(\hat{\tau}_x+i\hat{\tau}_y)l^{B_{2u}}$		$(1+tu_{2x})(1+C'_{21}u_{2z})\{\boldsymbol{D}''_3\times\tilde{\boldsymbol{A}}(\boldsymbol{e}_z)\}$
E_{1u}	E_{1u}-planar	$\hat{\tau}_x l_1^{E_{1u}}+\hat{\tau}_y l_2^{E_{1u}}$	$l_1^{E_{1u}}=(5k_z^2-1)k_x$	$(1+C'_{21}u_{2y}\tilde{\pi})\{{}_{II}\boldsymbol{D}_6\times T\}$
	E_{1u}-polar$_1$	$\hat{\tau}_z l_1^{E_{1u}}$	$l_2^{E_{1u}}=(5k_z^2-1)k_y$	$(1+C_{2z}\tilde{\pi})(1+C_{2z}u_{2x})\{\boldsymbol{C}'_{21}\times\boldsymbol{A}(\boldsymbol{e}_z)\times T\}$
	E_{1u}-polar$_2$	$\hat{\tau}_z l_2^{E_{1u}}$		$(1+C_{2z}\tilde{\pi})(1+C_{2z}u_{2x})\{\boldsymbol{C}''_{21}\times\boldsymbol{A}(\boldsymbol{e}_z)\times T\}$
	E_{1u}-bipolar	$\hat{\tau}_x l_1^{E_{1u}}+i\hat{\tau}_y l_2^{E_{1u}}$		$(1+tu_{2x})(1+C_{2z}\tilde{\pi})_{II}\boldsymbol{D}_2$
	E_{1u}-axial	$\hat{\tau}_z(l_1^{E_{1u}}+il_2^{E_{1u}})$		$(1+tC'_{21})(1+u_{2x}\tilde{\pi})\{\tilde{\boldsymbol{C}}_6\times\boldsymbol{A}(\boldsymbol{e}_z)\}$
	E_{1u}-β_1	$(\hat{\tau}_x+i\hat{\tau}_y)l_1^{E_{1u}}$		$(1+tu_{2x})(1+C_{2z}u_{2z})\{\boldsymbol{C}'_{21}\times\tilde{\boldsymbol{A}}(\boldsymbol{e}_z)\}$
	E_{1u}-β_2	$(\hat{\tau}_x+i\hat{\tau}_y)l_2^{E_{1u}}$		$(1+tu_{2x})(1+C_{2z}u_{2z})\{\boldsymbol{C}''_{21}\times\tilde{\boldsymbol{A}}(\boldsymbol{e}_z)\}$
	E_{1u}-γ	$(\hat{\tau}_x+i\hat{\tau}_y)(l_1^{E_{1u}}+il_2^{E_{1u}})$		$(1+tC'_{21}u_{2x})\{\tilde{\boldsymbol{C}}_6\times\tilde{\boldsymbol{A}}(\boldsymbol{e}_z)\}$
E_{2u}	E_{2u}-planar	$\hat{\tau}_x l_1^{E_{2u}}+\hat{\tau}_y l_2^{E_{2u}}$	$l_1^{E_{2u}}=2k_zk_xk_y$	$(1+C'_{21}u_{2x})(1+u_{2z}\tilde{\pi})\{{}_{II}\boldsymbol{C}_6^2\times T\}$
	E_{2u}-polar$_1$	$\hat{\tau}_z l_1^{E_{2u}}$	$l_2^{E_{2u}}=-k_z(k_x^2-k_y^2)$	$(1+u_{2x}\tilde{\pi})\{\boldsymbol{D}_2\times\boldsymbol{A}(\boldsymbol{e}_z)\times T\}$
	E_{2u}-polar$_2$	$\hat{\tau}_z l_2^{E_{2u}}$		$(1+u_{2x}\tilde{\pi})(1+C'_{21}u_{2x})\{\boldsymbol{C}_2\times\boldsymbol{A}(\boldsymbol{e}_z)\times T\}$
	E_{2u}-bipolar	$\hat{\tau}_x l_1^{E_{2u}}+i\hat{\tau}_y l_2^{E_{2u}}$		$(1+tu_{2x})(1+C'_{21}u_{2x})\boldsymbol{C}_2$
	E_{2u}-axial	$\hat{\tau}_z(l_1^{E_{2u}}+il_2^{E_{2u}})$		$(1+tC'_{21})\{\tilde{\boldsymbol{C}}_6^2\times\boldsymbol{A}(\boldsymbol{e}_z)\}$
	E_{2u}-β_1	$(\hat{\tau}_x+i\hat{\tau}_y)l_1^{E_{2u}}$		$(1+tu_{2x})\{\boldsymbol{D}_2\times\tilde{\boldsymbol{A}}(\boldsymbol{e}_z)\}$
	E_{2u}-β_2	$(\hat{\tau}_x+i\hat{\tau}_y)l_2^{E_{2u}}$		$(1+tu_{2x})(1+C'_{21}u_{2z})\{\boldsymbol{C}_2\times\tilde{\boldsymbol{A}}(\boldsymbol{e}_z)\}$
	E_{2u}-γ	$(\hat{\tau}_x+i\hat{\tau}_y)(l_1^{E_{2u}}+il_2^{E_{2u}})$		$(1+tC'_{21}u_{2x})\{\tilde{\boldsymbol{C}}_6^2\times\tilde{\boldsymbol{A}}(\boldsymbol{e}_z)\}$

$\tilde{\boldsymbol{A}}(\boldsymbol{e}_z)=\{u(\boldsymbol{e}_z,\theta)\tilde{\theta}|0\leq\theta\leq 2\pi\}$, $\boldsymbol{C}_2=\{E+C_{2z}\}$, $\boldsymbol{C}'_{21}=\{E+C'_{21}\}$, $\boldsymbol{D}'_3=\{\boldsymbol{C}_3+C'_{21}\boldsymbol{C}_3\}$, $\boldsymbol{D}''_3=\{\boldsymbol{C}_3+C''_{21}\boldsymbol{C}_3\}$, ${}_{II}\boldsymbol{D}_2=\{1,C_{2z}u_{2z},C'_{21}u_{2x},C''_{21}u_{2y}\}$, $\tilde{\boldsymbol{C}}_6=\{C_6^j(\frac{2\pi j}{6}),j=0,1,\cdots,5\}$, $\tilde{\boldsymbol{C}}_6^2=\{C_6^j(\frac{2\cdot 2\pi j}{6}),j=0,1,\cdots,5\}$, ${}_{II}\boldsymbol{C}_6^2=\{C_6^ju_6^{2j},j=0,1,\cdots,5\}$, $\hat{\tau}_\mu=i\hat{\sigma}_\mu\hat{\sigma}_y$ $(\mu=x,y,z)$.

phase $\boldsymbol{c}k_b(5k_c^2-1)$ as shown in Fig. 1. Thus the B phase is characterized by two horizontal line nodes at $\cos^2\theta=1/5$, or $\theta=63.4°$ and $116.6°$ and two point nodes at the poles (see Fig. 1(c)). The C (A) phase is the vertical line node at $k_b=0$ $(k_a=0)$ in addition to the two horizontal line nodes (see Fig. 1(c)). Thus it explains naturally the twofold thermal conductivity oscillation when H rotates within the basal plane. Note also that this gap structure with two line nodes and two point nodes in the B phase is consistent with a variety of transport measurements and bulk measurements mentioned above. In Fig. 2 we show the density of states (DOS) $N(E)$ for three phases.

B. Unitary versus non-unitary

It is seen from Table I that we list up the bipolar state given by $\hat{\tau}_x l_1^{E_{1u}}+i\hat{\tau}_y l_2^{E_{1u}}$ that is non-unitary and breaks the time reversal symmetry and that also can explain the phase diagram in H vs T. However, it is not consistent with the recent μSR experiment[48] that negates the earlier claim that the time reversal symmetry is broken[49]. The gap structure in this bipolar state is characterized by $|k_x\pm k_y||5k_z^2-1|$ in the B phase that has fourfold symmetry. This contradicts the thermal conductivity experiment[37] that indicated the rotational symmetry in the B phase.

C. Other classified states and strong SO state

The remaining states among the classified inert phase A_2, B_1, B_2, E_1 and E_2 are not accepted because of the following reasons: They do not provide the double transition (A_2, B_1, and B_2), or do not explain the twofold symmetry in the C phase (E_2). The other E_{1u} states in Table I are not appropriate except for the planar state, such as the polar$_1$, polar$_2$, axial, β_1, β_2, and γ either because they do not give the double transition (polar$_1$ and polar$_2$), or they fail to give an appropriate gap structure required (axial, β_1, β_2, and γ).

The E_{2u} $\boldsymbol{c}(k_a^2-k_b^2+2ik_ak_b)k_c$ classified in the strong SO case fails to explain the Knight shift experiment[24,25] and twofold symmetry in the C phase[37]. Then we are left with only E_{1u} planar state with the f-wave character mentioned above. Note also that since E_{1u} with the p-wave character $\hat{\tau}_xk_x+i\hat{\tau}_yk_y$ has no line node, it has been excluded as a candidate from the outset.

D. Dipole energy

The dipole energy

$$H_D\propto\left\langle 3|\boldsymbol{k}\cdot\boldsymbol{d}(\boldsymbol{k})|^2-|\boldsymbol{d}(\boldsymbol{k})|^2\right\rangle_{\boldsymbol{k}}, \tag{1}$$

depends on the combination of the spin and orbital states[50], where $\langle \cdots \rangle_{\boldsymbol{k}}$ indicates the Fermi surface average. The most favorable combinations by the dipole energy in E_{1u} state are $\boldsymbol{a}k_b(5k_c^2-1)$ and $\boldsymbol{b}k_a(5k_c^2-1)$. In the C phase, the spin state $\boldsymbol{b}$ is selected by the AF ordering and accompanies the orbital state $k_a(5k_c^2-1)$ by the dipole interaction. In the B phase, the remaining orbital state $k_b(5k_c^2-1)$ has to appear with the spin state $\boldsymbol{a}$ to minimize the dipole energy. However, the pairing state in the B phase without the magnetic field is $(\boldsymbol{b}k_a+\boldsymbol{c}k_b)(5k_c^2-1)$ actually (Fig. 1). Thus, the combination of the spin and orbital states cannot be interpreted from only the dipole energy.

III. QUASI-CLASSICAL EILENBERGER THEORY

We start with the quasi-classical spinful Eilenberger equation[51–55]. The quasi-classical Green's function $\widehat{g}(\boldsymbol{k},\boldsymbol{r},\omega_n)$ is calculated by the Eilenberger equation

$$-i\hbar\boldsymbol{v}(\boldsymbol{k})\cdot\boldsymbol{\nabla}\widehat{g}(\boldsymbol{k},\boldsymbol{r},\omega_n)=\left[\begin{pmatrix}[i\omega_n+(e/c)\boldsymbol{v}(\boldsymbol{k})\cdot\boldsymbol{A}(\boldsymbol{r})]\,\hat{1} & -\hat{\Delta}(\boldsymbol{k},\boldsymbol{r})\\ \hat{\Delta}(\boldsymbol{k},\boldsymbol{r})^{\dagger} & -[i\omega_n+(e/c)\boldsymbol{v}(\boldsymbol{k})\cdot\boldsymbol{A}(\boldsymbol{r})]\,\hat{1}\end{pmatrix},\widehat{g}(\boldsymbol{k},\boldsymbol{r},\omega_n)\right], \tag{2}$$

where the ordinary hat indicates the 2×2 matrix in spin space and the wide hat indicates the 4×4 matrix in particle-hole and spin spaces. The quasi-classical Green's function is described in particle-hole space by

$$\widehat{g}(\boldsymbol{k},\boldsymbol{r},\omega_n)=-i\pi\begin{pmatrix}\hat{g}(\boldsymbol{k},\boldsymbol{r},\omega_n) & i\hat{f}(\boldsymbol{k},\boldsymbol{r},\omega_n)\\ -i\hat{\underline{f}}(\boldsymbol{k},\boldsymbol{r},\omega_n) & -\hat{\underline{g}}(\boldsymbol{k},\boldsymbol{r},\omega_n)\end{pmatrix}, \tag{3}$$

with the direction of the relative momentum of a Cooper pair $\boldsymbol{k}$, the center-of-mass coordinate of the Cooper pair $\boldsymbol{r}$, and the Matsubara frequency $\omega_n=(2n+1)\pi k_BT$. The quasi-classical Green's function satisfies a normalization condition $\widehat{g}^2=-\pi^2\widehat{1}$. The Fermi velocity is assumed as $\boldsymbol{v}(\boldsymbol{k})=v_F\boldsymbol{k}$ on the three dimensional Fermi sphere. In the symmetric gauge the vector potential $\boldsymbol{A}(\boldsymbol{r})=(\bar{\boldsymbol{B}}\times\boldsymbol{r})/2+\boldsymbol{a}(\boldsymbol{r})$, where $\bar{\boldsymbol{B}}=(0,0,\bar{B})$ is a uniform flux density and $\boldsymbol{a}(\boldsymbol{r})$ is related to the internal field $\boldsymbol{B}(\boldsymbol{r})=\bar{\boldsymbol{B}}+\nabla\times\boldsymbol{a}(\boldsymbol{r})$. The unit cell of the vortex lattice is given by $\boldsymbol{r}=s_1(\boldsymbol{u}_1-\boldsymbol{u}_2)+s_2\boldsymbol{u}_2$ with $-0.5\le s_i\le0.5$ ($i=1,2$), $\boldsymbol{u}_1=(a_x,0,0)$, and $\boldsymbol{u}_2=(a_x/2,a_y,0)$. In this coordinate, a hexagonal lattice is described by $a_y/a_x=\sqrt{3}/2$ or $1/(2\sqrt{3})$.

Spin triplet order parameter is defined by

$$\hat{\Delta}(\boldsymbol{k},\boldsymbol{r})=i\boldsymbol{d}(\boldsymbol{k},\boldsymbol{r})\cdot\hat{\boldsymbol{\sigma}}\hat{\sigma}_y, \tag{4}$$

with

$$\boldsymbol{d}(\boldsymbol{k},\boldsymbol{r})=\boldsymbol{a}\Delta_a(\boldsymbol{r})\phi_a(\boldsymbol{k})+\boldsymbol{b}\Delta_b(\boldsymbol{r})\phi_b(\boldsymbol{k})+\boldsymbol{c}\Delta_c(\boldsymbol{r})\phi_c(\boldsymbol{k}), \tag{5}$$

where $\hat{\boldsymbol{\sigma}}$ is the Pauli matrix. The self-consistent condition for $\Delta_i(\boldsymbol{r})$ is given as

$$\begin{aligned}\hat{\Delta}(\boldsymbol{k},\boldsymbol{r})&=N_0\pi k_BT\\ &\times\sum_{0<\omega_n\le\omega_c}\left\langle V(\boldsymbol{k},\boldsymbol{k}')\left[\hat{f}(\boldsymbol{k}',\boldsymbol{r},\omega_n)+\hat{\underline{f}}^{\dagger}(\boldsymbol{k}',\boldsymbol{r},\omega_n)\right]\right\rangle_{\boldsymbol{k}'},\end{aligned} \tag{6}$$

where N_0 is the density of states in the normal state and ω_c is a cutoff energy setting $\omega_c=20\pi k_BT_c$ with the transition temperature T_c. We neglect the splitting of T_c because that is appropriate for low temperatures even in the B phase. The pairing interaction $V(\boldsymbol{k},\boldsymbol{k}')=g\phi(\boldsymbol{k})\phi(\boldsymbol{k}')^*$, where g is a coupling constant. The pairing functions $\phi(\boldsymbol{k})$ and $\phi_i(\boldsymbol{k})$ are chosen for each phase in UPt$_3$ appropriately. In our calculation, we use a relation

$$\frac{1}{gN_0}=\ln\frac{T}{T_c}+2\pi k_BT\sum_{0<\omega_n\le\omega_c}\frac{1}{\omega_n}. \tag{7}$$

The vector potential for the internal magnetic field $\boldsymbol{A}(\boldsymbol{r})$ is also self-consistently determined by

$$\begin{aligned}&\nabla\times[\nabla\times\boldsymbol{A}(\boldsymbol{r})]\\ &=8\pi\frac{e}{c}N_0 2\pi k_BT\sum_{0<\omega_n\le\omega_c}\langle\boldsymbol{v}(\boldsymbol{k})\,\mathrm{Im}\,[g_0(\boldsymbol{k},\boldsymbol{r},\omega_n)]\rangle_{\boldsymbol{k}},\end{aligned} \tag{8}$$

where g_0 is a component of the quasi-classical Green's function $\hat{g}$ in spin space, namely,

$$\hat{g}=\begin{pmatrix}g_0+g_z & g_x-ig_y\\ g_x+ig_y & g_0-g_z\end{pmatrix}.$$

We solve eq. (2) and eqs. (6) and (8) alternately, and obtain self-consistent solutions, under a given unit cell of the vortex lattice. The unit cell is divided to 41×41 mesh points, where we obtain the quasi-classical Green's functions, $\Delta_i(\boldsymbol{r})$, and $\boldsymbol{A}(\boldsymbol{r})$. When we solve eq. (2) by the Riccati method[56,57], we estimate $\Delta_i(\boldsymbol{r})$, and $\boldsymbol{A}(\boldsymbol{r})$ at arbitrary positions by the interpolation from their values at the mesh points, and by the periodic boundary condition of the unit cell including the phase factor due to the magnetic field[58–60]. In the numerical calculation, we use the units $R_0=\hbar v_F/(2\pi k_BT_c)$, $B_0=\hbar c/(2|e|R_0^2)$, and $E_0=\pi k_BT_c$ for length, magnetic field, and energy, respectively. By the dimensionless expression, eq. (8) is rewritten as

$$\begin{aligned}&\frac{R_0}{B_0}\nabla\times[\nabla\times\boldsymbol{A}(\boldsymbol{r})]\\&=-\frac{1}{\kappa^2}\frac{2T}{T_c}\sum_{0<\omega_n\leq\omega_c}\langle\boldsymbol{k}\ \mathrm{Im}\left[g_0(\boldsymbol{k},\boldsymbol{r},\omega_n)\right]\rangle_{\boldsymbol{k}},\end{aligned}\tag{9}$$

where $\kappa=B_0/(E_0\sqrt{8\pi N_0})=\sqrt{7\zeta(3)/18}\kappa_{\mathrm{GL}}$. We use a large GL parameter $\kappa_{\mathrm{GL}}=60$ owing to UPt$_3$.

By using the self-consistent solutions, free energy density is calculated by Luttinger-Ward thermodynamic potential[61] as

$$\begin{aligned}\delta\Omega=&N_0\frac{1}{gN_0}\left\langle\left\langle\frac{1}{2}\mathrm{Tr}\hat{\Delta}(\boldsymbol{k},\boldsymbol{r})\hat{\Delta}^\dagger(\boldsymbol{k},\boldsymbol{r})\right\rangle_{\boldsymbol{k}}\right\rangle_{\boldsymbol{r}}+N_0E_0^2\kappa^2\left\langle\left(\frac{\nabla\times\boldsymbol{A}(\boldsymbol{r})-\bar{\boldsymbol{B}}}{B_0}\right)^2\right\rangle_{\boldsymbol{r}}\\&-N_0\int_0^1 d\lambda\left\langle\pi k_BT\sum_{0<\omega_n\leq\omega_c}\left\langle\mathrm{Re}\left[\mathrm{Tr}\left\{\hat{\Delta}^\dagger(\boldsymbol{k},\boldsymbol{r})\left(\hat{f}_\lambda(\boldsymbol{k},\boldsymbol{r},\omega_n)+\underline{\hat{f}}^\dagger_\lambda(\boldsymbol{k},\boldsymbol{r},\omega_n)\right)\right\}\right]\right\rangle_{\boldsymbol{k}}\right\rangle_{\boldsymbol{r}},\end{aligned}\tag{10}$$

where $\langle\cdots\rangle_{\boldsymbol{r}}$ indicates the spatial average. The auxiliary functions $\hat{f}_\lambda$ and $\underline{\hat{f}}_\lambda$ are obtained by the substitution of $\lambda\hat{\Delta}$ for $\hat{\Delta}$ in eq. (2). This thermodynamic potential is relevant under large GL parameters and low magnetic fields because the replacement of the vector potential is not carried out.

DOS for energy E is given by

$$\begin{aligned}\bar{N}(E)=&\langle N(\boldsymbol{r},E)\rangle_{\boldsymbol{r}}\\=&\left\langle N_0\left\langle\mathrm{Re}\left[g_0(\boldsymbol{k},\boldsymbol{r},\omega_n)|_{i\omega_n\to E+i\eta}\right]\right\rangle_{\boldsymbol{k}}\right\rangle_{\boldsymbol{r}},\end{aligned}\tag{11}$$

where η is a positive infinitesimal constant and $N(\boldsymbol{r},E)$ is the local density of states (LDOS). Typically, we use $\eta=0.01\pi k_BT_c$. For obtaining $g_0(\boldsymbol{k},\boldsymbol{r},\omega_n)|_{i\omega_n\to E+i\eta}$, we solve eq. (2) with $\eta-iE$ instead of ω_n under the pair potential and vector potential obtained self-consistently.

IV. B PHASE

In the B phase, we take the pairing functions as $\phi=\sqrt{21/8}(k_a+k_b)(5k_c^2-1)$, $\phi_b=\sqrt{21/8}k_a(5k_c^2-1)$, and $\phi_a=\phi_c=\sqrt{21/8}k_b(5k_c^2-1)$, where one component of the d-vector is directed toward the b-axis and the other can rotate in the ac-plane.

A. Double-core vortex lattice

The pairing function in the B phase is similar to that in the superfluid ^{3}He B-phase, namely $\boldsymbol{d}(\boldsymbol{k})\propto\boldsymbol{x}k_x+\boldsymbol{y}k_y+\boldsymbol{z}k_z$[62]. Owing to the analogy with the ^{3}He B-phase, there is the possibility that the unconventional double-core vortex[63,64] and v vortex[65,66] with a chiral core are stabilized against the conventional singular vortex. In fact, double-core vortex and v vortex are stabilized in the low and high pressure regions, respectively, in the ^{3}He B-phase[63,64]. Under our pairing function in the UPt$_3$ B phase, the v (chiral core) vortex lattice is not stabilized self-consistently; however, there are two types of the self-consistent vortex lattice, namely, the hexagonal singular vortex lattice and the double-core vortex lattice.

At $T=0.2T_c$ under $\bar{B}=0.05B_0$ to the c-axis, spatial variation of the pair potential amplitude for the singular vortex lattice and the double-core vortex lattice is shown in Figs. 3(a) and 3(b)-(d), respectively, where the total pair potential is defined by $|\Delta(\boldsymbol{r})|\equiv\sqrt{\langle\mathrm{Tr}[\hat{\Delta}(\boldsymbol{k},\boldsymbol{r})^\dagger\hat{\Delta}(\boldsymbol{k},\boldsymbol{r})]/2\rangle_{\boldsymbol{k}}}$. Since the pair potential is axisymmetric for the c-axis in the B phase, conventional singular vortices form a perfect hexagonal lattice (Fig. 3(a)). By contrast, a double-core vortex spontaneously breaks the axisymmetry. Schematic structure of the double-core vortex by d-vector is shown in Fig. 3(e). The OP in the bulk is depicted by the blue (black) and red (gray) arrows which indicate d-vector with the orbital states $\lambda_a=\sqrt{21/8}k_a(5k_c^2-1)$ and $\lambda_b=\sqrt{21/8}k_b(5k_c^2-1)$, respectively. Along the b-axis across the vortex center, the red (gray) arrow rotates in the ac-plane from the c direction far from the vortex to the $-c$ direction at the opposite side of the vortex via the a direction at the vortex center. On the other hand, the blue (black) arrow directed toward the b direction is shortened as approaching the vortex center and finally vanishes at the vortex center; then, across the vortex center, the arrow is lengthened toward the $-b$ direction to the initial length as far from the vortex. Thus, since d-vector can be modulated continuously across the vortex center, there is not the singularity where the total amplitude vanishes. Instead of the singularity, the double-core with the small amplitude $\approx 0.6E_0$ exist as shown by contour lines in Fig. 3(b). This double-core has phase winding π same as in the half-quantum vortex[67].

By the spontaneously broken axisymmetry, the double-core vortex lattice is distorted. The stable ratio between the height and base of the triangular lattice is $a_y/a_x=\sqrt{3}/2.4$, namely a base angle $\alpha\equiv\tan^{-1}(2a_y/a_x)\approx 55°$. Each component of the double-core vortex lattice is also shown in Figs. 3(c) and 3(d) for the amplitude of the bulk components $|\Delta_b(\boldsymbol{r})| = |\Delta_c(\boldsymbol{r})|$ and that of the compensating component at the vortex cores $|\Delta_a(\boldsymbol{r})|$, respectively. The vortex core in the bulk component is slightly elliptic with the line of apsides along the a-axis and the compensating component is enlarged along the b-axis. Since the vortex lattice tends to avoid the overlap of the vortex cores and that of the compensating component, the stable structure is fixed by the competition between them.

At these low temperature and low magnetic field, the double-core vortex is more stable than the singular vortex. At high temperatures, however, the double-core vortex is unstable against the singular vortex because the compensating component tends to connect with the neighbor vortices along the b-axis by the extension of the coherence length. Similarly, under high magnetic fields, since the distance between the vortex centers becomes short, the double-core vortex is unstable. The Pauli-paramagnetic effect, which rotates the d-vector under $H > H_{\rm rot}$, is neglected in this calculation. Since the compensating component of the d-vector for $\boldsymbol{b}\lambda_a + \boldsymbol{a}\lambda_b$ has to be directed toward the c-axis, the double-core vortex is unstable under high magnetic fields $H > H_{\rm rot}$ also by the Pauli-paramagnetic effect.

By the measurement of the small-angle neutron scattering (SANS), the perfect hexagonal lattice with $\alpha = 60°$ is observed in the B phase[68]. Thus, the observed vortices are conventional singular vortices. Since this experiment is carried out under the magnetic field $H \approx H_{\rm rot}$, the double-core vortex may be unstable by the Pauli-paramagnetic effect.

B. Local density of states

There are clear differences in the LDOS between the double-core vortex lattice and the singular vortex lattice, which can be directly measured in scanning tunneling microscopy/spectroscopy (STM/STS). The LDOS for the double-core vortex lattice and the singular vortex lattice is shown in Figs. 4 and 5, respectively. The zero energy peak is expanded to the region between the double-core (Fig. 4(a)) because the local OP $\boldsymbol{a}\lambda_b$ in this region has a line node in the ac-plane. Besides, there is the elliptic peak extending toward the a-axis in the LDOS at $E = 0.1E_0$ (Fig. 4(b)). By contrast, the singular vortex has an isotropic peak in the LDOS at $E = 0$ and $E = 0.1E_0$ (Figs. 5(a) and 5(b)). Spectral evolution of the LDOS near the vortex also differs between the double-core vortex lattice and the singular vortex lattice. Near the double-core vortex center, there is a sharp low energy peak especially along the a-axis (Figs. 4(c) and 4(e)) and along the b-axis which is somewhat round (Figs. 4(d) and 4(f)). In the double-core case the OP two minima are situated just outside the center along the a-axis (see Fig. 3(b)), giving rise to sharp peaks at a finite energy as seen from Fig. 4(e). On the other hand, the zero energy peak is varied to a bump away from the vortex core for the singular vortex (Figs. 5(c)-5(f)). It is noted that in the bulk region away from the vortex core the DOS $\propto |E|^2$ at low energy as seen from Figs. 4(d) and 5(d) because the gap structure is characterized by two point nodes and two line nodes. This is also seen from Fig. 2.

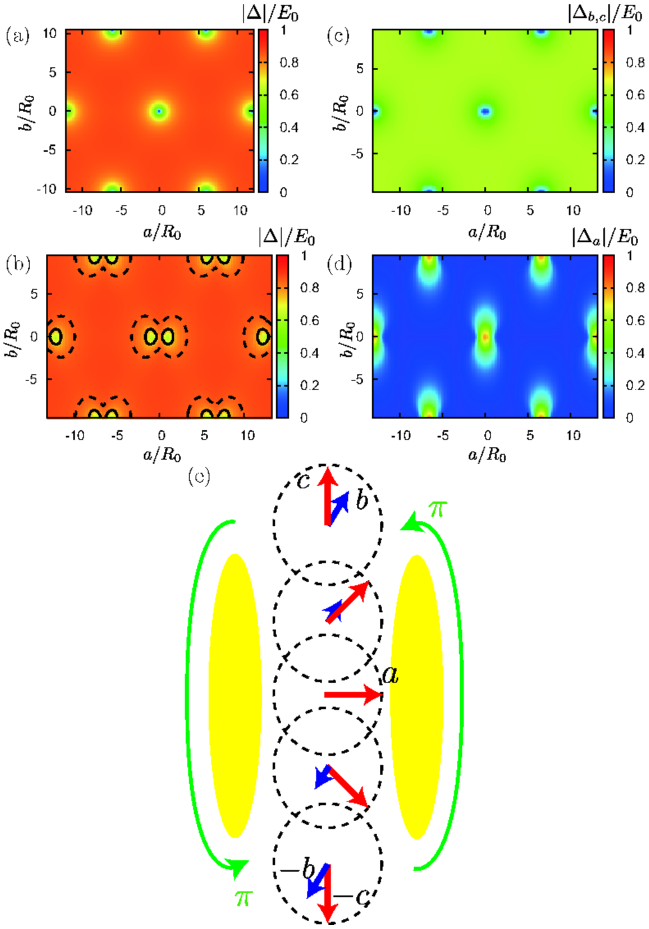

FIG. 3. (Color online) Spatial variation of the pair potential at $T = 0.2T_c$ under $\bar{B} = 0.05B_0$ for the hexagonal singular vortex lattice (a) and for the double-core vortex lattice with $\alpha \approx 55°$ (b)-(d). (a) Amplitude of the total pair potential $|\Delta(\boldsymbol{r})|$, (b) amplitude of the total pair potential $|\Delta(\boldsymbol{r})|$ with the contour lines on $0.75E_0$ (solid lines) and $0.85E_0$ (dashed lines), (c) amplitude of the bulk components $|\Delta_b(\boldsymbol{r})| = |\Delta_c(\boldsymbol{r})|$, (d) amplitude of the compensating component at the vortex cores $|\Delta_a(\boldsymbol{r})|$, and (e) schematic spin structure of the double-core vortex around the core.

C. NMR spectrum

The double-core vortex lattice is also observed by the NMR measurement. In the NMR experiment, the resonance frequency spectrum of the nuclear spin resonance is determined by the internal magnetic field. The distri-

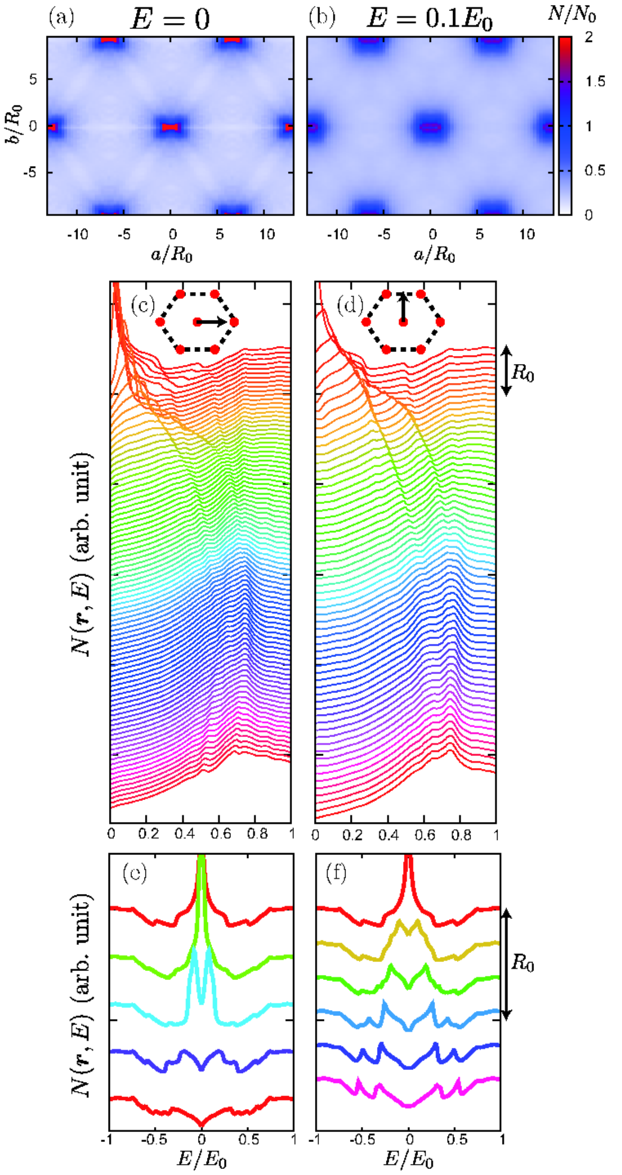

FIG. 4. (Color online) LDOS at $T = 0.2T_c$ under $\bar{B} = 0.05B_0$ for the double-core vortex lattice. Spatial variation of the LDOS at $E = 0$ (a) and $E = 0.1E_0$ (b). Spectral evolution of the LDOS from the vortex center (top) along the a-axis (c) and b-axis (d). Details of the evolution near the vortex center are shown in (e) and (f), respectively.

bution function is given by

$$P(B) = \int \delta[B - B_c(\boldsymbol{r})] d\boldsymbol{r}, \qquad (12)$$

i.e., volume counting for B in a unit cell. This resonance line shape is called the "Redfield pattern" of the vortex lattice. In Fig. 6, we show the distribution functions $P(B)$ for the singular vortex lattice (dashed line) and for the double-core vortex lattice (solid line). The distribution function for the singular vortex lattice has a single peak at $B = 0.049969B_0$. This peak comes from the outside of the vortex core shown by the contour lines in the left inset of Fig. 6. By contrast, the distribution function for the double-core vortex lattice has a double peak at $B = 0.049962B_0$ and $B = 0.049975B_0$. The peaks at the low and high fields come from outside the vortex (solid line) and around the vortex (dashed line), respectively, shown by the contour lines in the right inset of Fig. 6. The distortion of the double-core vortex lattice gives a clear difference in the NMR spectrum.

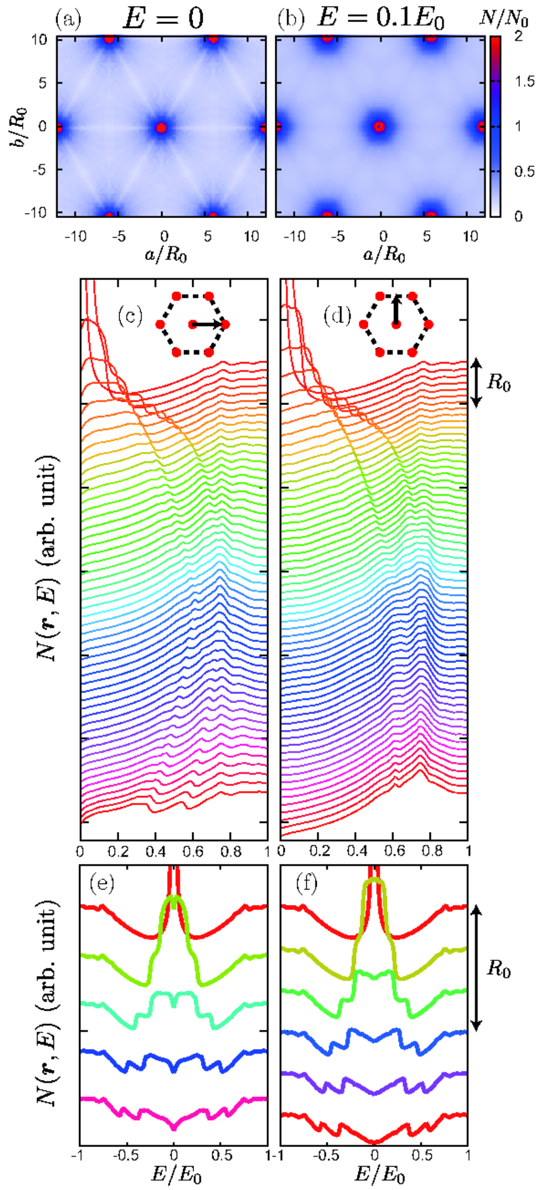

FIG. 5. (Color online) LDOS at $T = 0.2T_c$ under $\bar{B} = 0.05B_0$ for the singular vortex lattice. Spatial variation of the LDOS at $E = 0$ (a) and $E = 0.1E_0$ (b). Spectral evolution of the LDOS from the vortex core (top) along the a-axis (c) and b-axis (d). Details of the evolution near the vortex core are shown in (e) and (f), respectively.

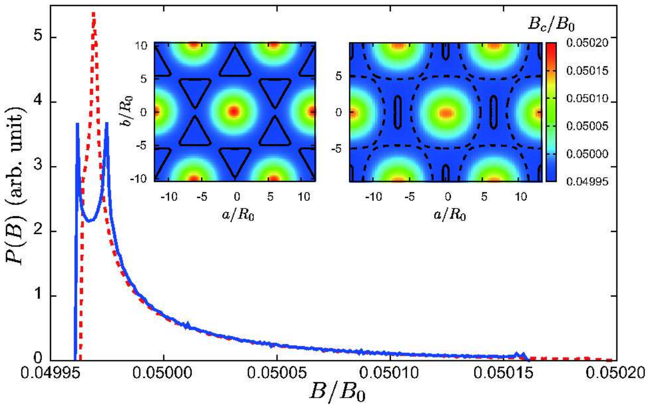

FIG. 6. (Color online) Distribution functions of the internal magnetic field $P(B)$ at $T = 0.2T_c$ under $\bar{B} = 0.05B_0$ for the singular vortex lattice (dashed line) and for the double-core vortex lattice (solid line). The height of $P(B)$ is scaled so that $\int P(B)dB = 1$. Inset: Spatial variation of the internal magnetic field $B_c(\boldsymbol{r})$ for the singular vortex lattice (left) and for the double-core vortex lattice (right) with the contour lines on the magnetic field situated at the peaks of $P(B)$.

V. C AND A PHASES

In the C phase, we take the pairing functions as $\phi = \phi_a = \sqrt{21/8}k_b(5k_c^2 - 1)$ and $\phi_b = \phi_c = 0$, where the pair potential has one spin component. Note that the A phase is same as the C phase except that the a- and b-axes are exchanged.

A. Morphology of vortex lattice

In this section, we discuss the deformation of the vortex lattice in the C phase under $H \parallel c$ to see the effects of the twofold gap function $\boldsymbol{d}(\boldsymbol{k}) \propto \boldsymbol{a}k_b(5k_c^2 - 1)$. Since the vortex cores are extended along the antinodal b direction, the height of the triangular lattice is enlarged along the b direction to avoid the overlap of the vortex cores. This variation of the vortex lattice is also same for the A phase by rotating it in the ab-plane. To find the stable vortex lattice, we compare the free energy among the triangular lattices with various ratios between the height and base, namely a_y/a_x.

We show the stable vortex lattices under a low magnetic field $\bar{B} = 0.02B_0$ in Figs. 7(a)-7(c) and a high magnetic field $\bar{B} = 0.3B_0$ in Figs. 7(d)-7(f). These figures are also shown at different temperatures which are at a low temperature $T = 0.2T_c$ in Figs. 7(a) and 7(d), at an intermediate temperature $T = 0.5T_c$ in Figs. 7(b) and 7(e), and at a high temperature $T = 0.7T_c$ in Figs. 7(c) and 7(f). The triangular lattice is slightly distorted under the low magnetic field at the low temperature shown in Fig. 7(a). In this case, the ratio is $a_y/a_x = 0.6\sqrt{3}$, that is, a base angle of the isosceles triangular lattice is $\alpha \equiv \tan^{-1}(2a_y/a_x) \approx 64°$. As temperature increases, the stable structures of the vortex lattice are $a_y/a_x = 0.65\sqrt{3}$, namely $\alpha \approx 66°$ (Fig. 7(b)) and $a_y/a_x = 0.8\sqrt{3}$, namely $\alpha \approx 70°$ (Fig. 7(c)). The vortex lattice is distorted drastically under the high magnetic field. At the low temperature, the stable structure is $a_y/a_x = 0.95\sqrt{3}$, namely $\alpha \approx 73°$ shown in Fig. 7(d). Physically, the maximally distorted triangular lattice is $a_y/a_x = \sqrt{17}/2$, namely $\alpha \approx 76°$ beyond which some of the nearest neighbors are no longer nearest. Since the distortion of the triangular lattice is near the limit even at the low temperature, the vortex lattice is hardly distorted by the increase of temperature as shown in Figs. 7(e) and 7(f) where $a_y/a_x = \sqrt{3}$, namely $\alpha \approx 74°$. Thus, the vortex lattice tends to be more distorted to avoid the overlap of the vortex cores under high magnetic fields and at high temperatures because the ratio of the radius of the vortex core proportional to the coherence length $\xi \propto (T_c - T)^{-1/2}$ to the distance between the vortices proportional to $\bar{B}^{-1/2}$ increases. The deformation of the vortex lattice is summarized in Fig. 7(g).

However, the regular hexagonal vortex lattice was observed in the A phase by the measurement of the SANS[68]. In this experiment, since the vortex lattice in the A phase is observed at the low temperature in which the B phase appears by the rapid cooling, the observed vortex lattice may change to the hexagonal singular vortex lattice in the B phase mentioned before.

B. Local density of states

The twofold symmetry of the gap function is revealed as shown in Fig 8 where the LDOS is displayed. The zero energy LDOS (Fig. 8(a)) is well connected between nearest-neighbor vortices along the a-axis which is the nodal direction. The LDOS at $E = 0.1E_0$ (Fig. 8(b)) is also well connected between the nearest-neighbor vortices, and moreover, it has two peaks within a unit cell aligned along the b-axis. Spectral evolution of the LDOS along the a-axis (Figs. 8(c) and 8(e)) forms the peak structure at a low energy near the vortex core. At few $R_0 \sim \xi$ away from the vortex core, the spectra still increase from the zero energy so as to make a low energy peak. On the other hand, it has a rounded bump near the vortex core along the b-axis (Figs. 8(d) and 8(f)). At few R_0 away from the vortex core, the low energy spectra are almost flat. Far from the vortex core, their spectra become the same structure at the middle point between the vortex cores. It is noted that in the bulk region away from the vortex core the DOS $\propto |E|$ at low energy as seen from Fig. 8(d) because the gap structure is characterized by one vertical and two horizontal line nodes. This is also seen from Fig. 2.

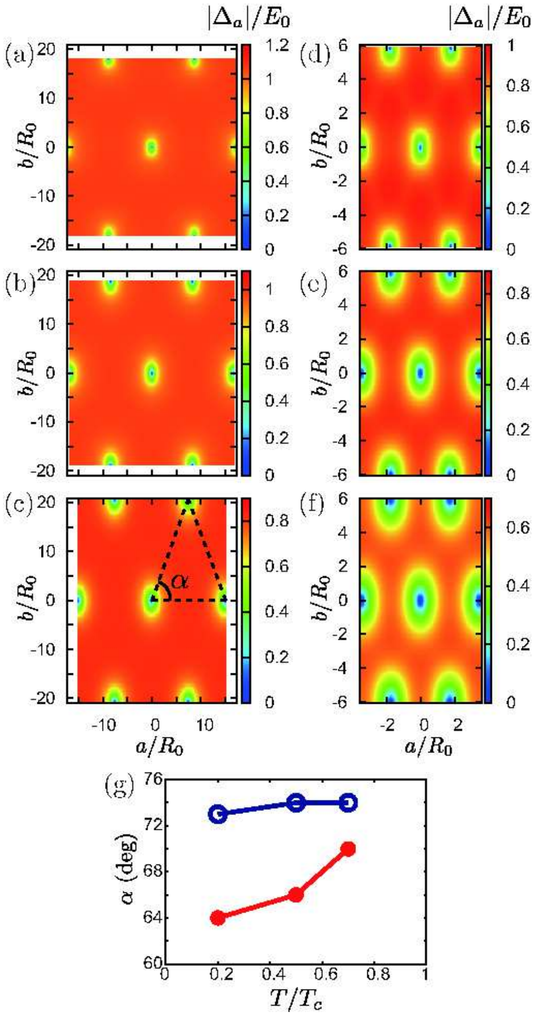

FIG. 7. (Color online) (a)-(f) Spatial variation of the stable pair potential amplitude $|\Delta_a(\boldsymbol{r})|$. (a) $\alpha \approx 64^\circ$ under $\bar{B} = 0.02B_0$ at $T = 0.2T_c$, (b) $\alpha \approx 66^\circ$ under $\bar{B} = 0.02B_0$ at $T = 0.5T_c$, (c) $\alpha \approx 70^\circ$ under $\bar{B} = 0.02B_0$ at $T = 0.7T_c$, (d) $\alpha \approx 73^\circ$ under $\bar{B} = 0.3B_0$ at $T = 0.2T_c$, (e) $\alpha \approx 74^\circ$ under $\bar{B} = 0.3B_0$ at $T = 0.5T_c$, and (f) $\alpha \approx 74^\circ$ under $\bar{B} = 0.3B_0$ at $T = 0.7T_c$. (g) Temperature dependence of the base angle α under $\bar{B} = 0.02B_0$ (solid circles) and $\bar{B} = 0.3B_0$ (open circles).

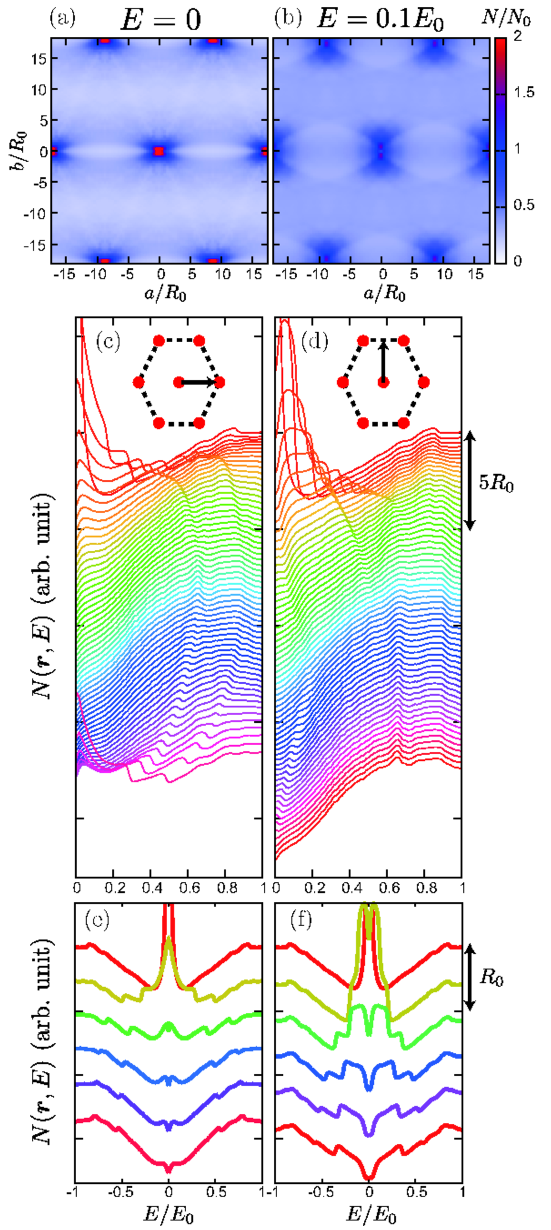

FIG. 8. (Color online) LDOS at $T = 0.2T_c$ under $\bar{B} = 0.02B_0$ in the C phase. Spatial variation of the LDOS at $E = 0$ (a) and $E = 0.1E_0$ (b). Spectral evolution of the LDOS from the vortex core (top) along the a-axis (c) and b-axis (d). Details of the evolution near the vortex core are shown in (e) and (f), respectively.

C. Field angle-resolved zero energy density of states

We analyze the field angle-resolved thermal conductivity experiment[37] according to the identified pair function. In this experiment, since the temperature dependence of thermal conductivity obeys the Wiedemann-Franz law at low temperatures, the most significant effect on the thermal transport in the vortex state comes from the Doppler shift of the QP energy spectrum, $E(\boldsymbol{p}) \to E(\boldsymbol{p}) - \boldsymbol{v}_s \cdot \boldsymbol{p}$, in the circulating supercurrent flow $\boldsymbol{v}_s$. This effect becomes important at such positions where the gap becomes smaller than the Doppler shift term ($|\Delta| < \boldsymbol{v}_s \cdot \boldsymbol{p}$). Since the magnitude of the Doppler shift strongly depends on the angle between the nodal direction and the magnetic field, the oscillation of zero energy DOS occurs. Consequently, thermal conductivity attains the maximum (minimum) value when the magnetic field is directed to the antinodal (nodal) directions[69–71]. In this experiment, however, since heat current is injected along the c-axis, thermal conductivity cannot be compared to zero energy DOS directly. Then, we compare differences

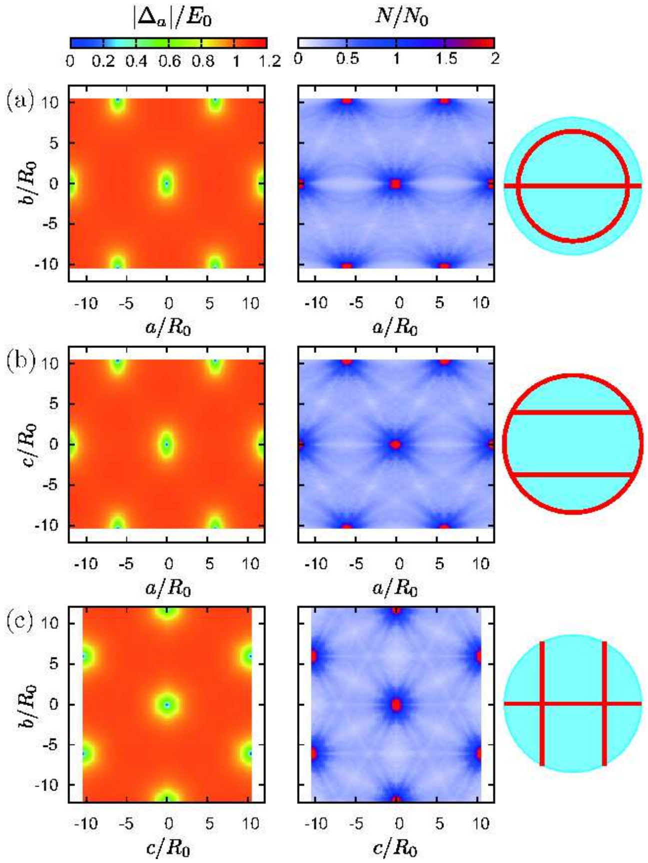

FIG. 9. (Color online) Spatial variation of the pair potential amplitude $|\Delta_a(\boldsymbol{r})|$ and the zero energy LDOS $N(\boldsymbol{r}, E=0)$ at $T = 0.2T_c$ under $\bar{B} = 0.05B_0$. The magnetic fields are directed to the c-axis (a), b-axis (b), and a-axis (c). Left (middle) panels show the OP amplitude (zero energy LDOS). Right panels show a schematic view of line nodes seen from the field direction.

of them when field directions are rotated along the vertical line node and antinode in the C phase.

In this section, we assume a regular hexagonal vortex lattice $a_y/a_x = \sqrt{3}/2$ or $1/(2\sqrt{3})$. The stable orientation of the vortex lattice is determined by comparing the free energy calculated by eq. (10). At $T = 0.2T_c$ under $\bar{B} = 0.05B_0$, the spatial variations of the pair potential amplitude and the zero energy LDOS are shown in left panels and middle panels of Figs. 9(a)-9(c), respectively. When the magnetic field is directed to the c-axis (Fig. 9(a)) or b-axis (Fig. 9(b)), elliptic vortex cores shrink to the vertical ($H \parallel c$) or tropical ($H \parallel b$) nodal directions. Under these magnetic fields, zero energy LDOS is mainly connected between nearest-neighbor vortices along the a-axis. On the other hand, under $H \parallel a$ (Fig. 9(c)), since the vertical node and the tropical nodes have a similar contribution to the QPs, vortex cores are hexagonal and zero energy LDOS is well connected among all nearest-neighbor vortices, giving rise to a rather round core profile in Fig. 9(c).

By taking the spatial average of the zero energy LDOS under various field directions, the field angle-resolved zero energy DOS is obtained shown in Fig. 10(a). When field direction is rotated along the vertical line node from the c-axis (open circles), the zero energy DOS is diminished because the low energy excitations from the tropical line nodes decrease. Within $45^\circ < \theta < 60^\circ$ and $120^\circ < \theta < 135^\circ$, the orientation of the vortex lattice changes, that is, the nearest-neighbor vortices are aligned along the b-axis in $60^\circ \leq \theta \leq 120^\circ$ and next-nearest-neighbor vortices are aligned along the b-axis in $\theta \leq 45^\circ, 135^\circ \leq \theta$. By contrast, when magnetic field is rotated along the antinodal direction (solid circles), the zero energy DOS is almost constant because the QPs mainly come from the tropical line nodes under $H \parallel c$ and from the vertical line node under $H \parallel b$. The difference of the zero energy DOS between the fields along the vertical line node and antinode is maximum on the equator $\theta = 90^\circ$ because the horizontal line nodes are situated on the tropics. This θ-dependence of the difference of the zero energy DOS is consistent with the measurement of thermal conductivity[37], shown in Fig. 10(b). Earlier spin singlet d-wave E_{1g} model ($\phi = \sqrt{15}k_b k_c$) and spin triplet f-wave E_{2u} model ($\phi = \phi_c = \sqrt{105}k_a k_b k_c,\ \phi_a = \phi_b = 0$)[7], however, have two peaks of the difference of the zero energy DOS at $\theta \neq 90^\circ$ by the equatorial line node.

VI. CONCLUSION AND PERSPECTIVES

In this paper we have classified possible pairing functions under the given crystalline symmetry D_{6h} for the heavy fermion superconductor UPt$_3$, which belong to the f-wave character with the triplet channel. Then we identified a planar spin triplet state among them that maximally fits to the existing experiments, in particular:

(A) Various bulk thermodynamic measurements that indicate the line node(s) and point node(s) in the B phase.

(B) The Knight shift experiment that shows the two field directions where the Knight shift decreases below T_c, implying that the d-vector contains the $\boldsymbol{b}$-component and $\boldsymbol{c}$-component at lower fields and the d-vector rotates from $\boldsymbol{c}$ to $\boldsymbol{a}$ at $H_{\rm rot}$ ($\parallel c$) ~ 2 kG.

(C) The angle-resolved thermal conductivity measurement shows twofold gap structure in the C phase and rotational symmetry in the B phase.

Those important experimental facts are all explained by the planar state with the f-wave channel, namely, $(\boldsymbol{c}k_b + \boldsymbol{b}k_a)(5k_c^2 - 1)$.

In order to check our proposed state, we made several predictions that are calculated by solving the microscopic Eilenberger equation with our planar state. The predictions include

(1) The vortex structure in the C phase and likewise A phase exhibit strong distorted triangular lattice that varies as functions of T and H when $H \parallel c$. This distortion is caused by the twofold gap structures in the A and

TABLE II. Candidate pair functions.

irr. rep.	basis	Knight shift	point + line	twofold in C	gradient coupling
E_{1g}	$k_z(k_x, k_y)$	×	◯	◯	×
E_{2g}	$(k_x^2 - k_y^2, k_x k_y)$	×	×	×	△
E_{1u}^p	$\boldsymbol{z}(k_x, k_y)$	△	×	◯	×
E_{2u}	$\boldsymbol{z}(k_x^2 - k_y^2, k_x k_y)k_z$	△	◯	×	△
E_{1u}^f	$(\boldsymbol{x}k_y, \boldsymbol{y}k_x)(5k_z^2 - 1)$	◯	◯	◯	◯

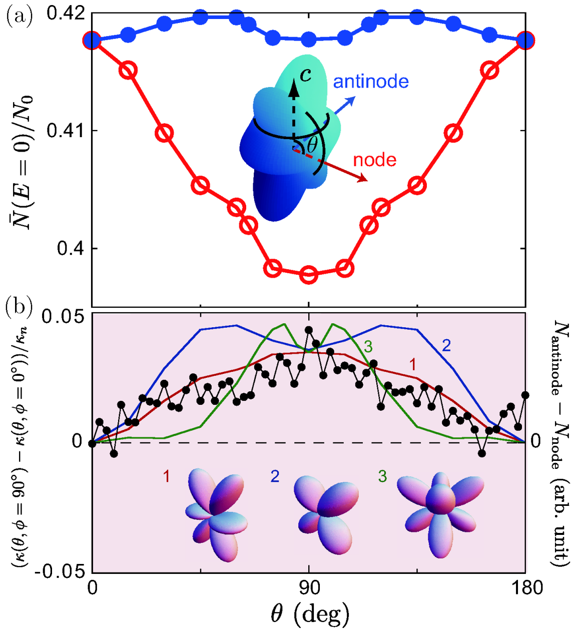

FIG. 10. (Color online) (a) Field angle-resolved zero energy DOS at $T = 0.2T_c$ under $\bar{B} = 0.05B_0$. The field directions are rotated along the vertical line node (open circles) and antinode (solid circles) as schematically shown in the inset. (b) θ-dependence of the thermal conductivity normalized by the normal state value κ_n (left axis) and the DOS difference normalized at $\theta = 90°$ (right axis) along the vertical nodal and antinodal scanning for three possible gap functions in the C phase: 1. The present E_{1u} $(k_b(5k_c^2-1))$, 2. E_{1g} $(k_b k_c)$, 3. E_{2u} $(k_a k_b k_c)$. The gap structures are sketched in the inset. The experimental data are taken from ref. 37.

C phases. The vortex morphology should be observed by SANS experiment.

(2) While in the A and C phases the vortices are all singular, that is, the OP vanishes at the core because of the single component OP, in the B phase the vortex is non-singular characterized by the double core structure. To check this complex vortex structure, we provide several signatures, such as the magnetic field distribution probed as the resonance spectrum of NMR and the LDOS around a vortex core probed by STM/STS.

A. Comparison with other proposed states

There are several proposals to identify the pairing symmetries in UPt$_3$. The E_{1g} and E_{2g} are singlet and unable to explain the Knight shift experiment mentioned above. The E_{1u}^p with the p-wave character is not accepted because there is no line node whose existence is firmly established through various thermodynamic experiments. The E_{2u} which was regarded as most promising candidate contradicts the observed twofold gap structure in the C phase. Table II summarizes the present status of various candidates.

B. Remaining issues

There remain several issues to be answered.

(1) The d-vector rotation

In order to understand the d-vector rotation phenomenon at $H_{\rm rot} \sim 2$ kG for $H \parallel c$, we need to take into account the magnetic field energy due to the anisotropic susceptibility in the superconducting state. In the absence of this effect the induced component $\boldsymbol{a}$ near the vortex core center in the double-core phase decreases as the vortex distance decreases.

(2) The origin of the symmetry breaking

To split T_c into T_{c1} and T_{c2}, we need some symmetry breaking field. The good candidate is the AF order at $T_N = 5$ K observed by neutron scattering. This is a high energy probe to catch the instantaneous correlation as a snap shot. Other low energy probes, such as NMR and μSR fail to observe the static AF order. Since a precise correlation between the AF order and the T_c splitting under pressure, which simultaneously disappear at $P \sim 3$ kbar, is observed[72], this is still a puzzling although we presented previously a scenario for this splitting due to AF fluctuations[15]. An alternative idea is to invoke the crystal symmetry lowering that is also reported before[73–76].

(3) Pairing mechanism

As mentioned in Sec. II the dipole energy alone cannot explain the stability of the pairing form $(\boldsymbol{c}k_b + \boldsymbol{b}k_a)(5k_c^2 - 1)$. This special combination between the spin direction and the orbital form is rooted to the pairing mechanism. This is a main issue to be explore for future since now the pairing symmetry is determined in this paper.

(4) Topological aspect

The identified pairing state $(\boldsymbol{c}k_b+\boldsymbol{b}k_a)(5k_c^2-1)$ is analogous to the superfluid ^{3}He B-phase whose form is described as $\boldsymbol{x}k_x+\boldsymbol{y}k_y+\boldsymbol{z}k_z$ realized in the bulk or the planar state $\boldsymbol{x}k_x+\boldsymbol{y}k_y$ realized in thin films. Our state has the Majorana particles in the boundary as an Andreev bound state albeit the line and point nodes exist in the bulk. This is interesting because recently Sato argues a possibility of the topological protection under the nodal gap[77] The topological nature is discussed in a similar situation in connection with the superfluid ^{3}He A-phase where the Majorana particles exist in the point node gap[78,79]. This topological aspect certainly deserves further investigation. Note that the double-core vortex does not contain the Majorana zero mode.

ACKNOWLEDGMENTS

We thank K. Izawa, Y. Machida, T. Sakakibara, and S. Kittaka for informative discussions on their experiments and M. Ichioka for formulations and computational coding. This work was supported by JSPS, KAKENHI (No. 21340103). Y.T. acknowledges the support of the Research Fellowships of JSPS for Young Scientists.

---

[1] G. R. Stewart, Z. Fisk, J. O. Willis, and J. L. Smith: Phys. Rev. Lett. **52** (1984) 679.

[2] R. A. Fisher, S. Kim, B. F. Woodfield, N. E. Phillips, L. Taillefer, K. Hasselbach, J. Flouquet, A. L. Giorgi, and J. L. Smith: Phys. Rev. Lett. **62** (1989) 1411.

[3] K. Hasselbach, L. Taillefer, and J. Flouquet: Phys. Rev. Lett. **63** (1989) 93.

[4] G. Bruls, D. Weber, B. Wolf, P. Thalmeier, B. Lüthi, A. d. Visser, and A. Menovsky: Phys. Rev. Lett. **65** (1990) 2294.

[5] A. Schenstrom, M. F. Xu, Y. Hong, D. Bein, M. Levy, B. K. Sarma, S. Adenwalla, Z. Zhao, T. Tokuyasu, D. W. Hess, J. B. Ketterson, J. A. Sauls, and D. G. Hinks: Phys. Rev. Lett. **62** (1989) 332.

[6] J. A. Sauls: Adv. Phys. **43** (1994) 113.

[7] R. Joynt and L. Taillefer: Rev. Mod. Phys. **74** (2002) 235.

[8] R. Joynt: Supercond. Sci. Technol. **1** (1988) 210.

[9] K. Machida and M. Ozaki: J. Phys. Soc. Jpn. **58** (1989) 2244.

[10] K. Machida, M. Ozaki, and T. Ohmi: J. Phys. Soc. Jpn. **58** (1989) 4116.

[11] K. Machida and M. Ozaki: Phys. Rev. Lett. **66** (1991) 3293.

[12] M. Ozaki and K. Machida: J. Phys. Soc. Jpn. **61** (1992) 1277.

[13] D. W. Hess, T. A. Tokuyasu, and J. A. Sauls: J. Phys.: Condens. Matter **1** (1989) 8135.

[14] T. A. Tokuyasu, D. W. Hess, and J. A. Sauls: Phys. Rev. B **41** (1990) 8891.

[15] K. Machida and T. Ohmi: J. Phys. Soc. Jpn. **65** (1996) 3456.

[16] J. A. Sauls: J. Low Temp. Phys. **95** (1994) 153.

[17] T. Ohmi and K. Machida: Phys. Rev. Lett. **71** (1993) 625.

[18] K. Machida, T. Ohmi, and M. Ozaki: J. Phys. Soc. Jpn. **62** (1993) 3216.

[19] K. Machida, T. Ohmi, and M. Ozaki: J. Phys. Soc. Jpn. **64** (1995) 1067.

[20] T. Ohmi and K. Machida: J. Phys. Soc. Jpn. **65** (1996) 4018.

[21] K. Machida, T. Nishira, and T. Ohmi: J. Phys. Soc. Jpn. **68** (1999) 3364.

[22] C. H. Choi and J. A. Sauls: Phys. Rev. Lett. **66** (1991) 484.

[23] C. H. Choi and J. A. Sauls: Phys. Rev. B **48** (1993) 13684.

[24] H. Tou, Y. Kitaoka, K. Asayama, N. Kimura, Y. Ōnuki, E. Yamamoto, and K. Maezawa: Phys. Rev. Lett. **77** (1996) 1374.

[25] H. Tou, Y. Kitaoka, K. Ishida, K. Asayama, N. Kimura, Y. Ōnuki, E. Yamamoto, Y. Haga, and K. Maezawa: Phys. Rev. Lett. **80** (1998) 3129.

[26] B. Lussier, L. Taillefer, W. J. L. Buyers, T. E. Mason, and T. Petersen: Phys. Rev. B **54** (1996) R6873.

[27] H. Suderow, J. Brison, A. Huxley, and J. Flouquet: J. Low Temp. Phys. **108** (1997) 11.

[28] D. J. Bishop, C. M. Varma, B. Batlogg, E. Bucher, Z. Fisk, and J. L. Smith: Phys. Rev. Lett. **53** (1984) 1009.

[29] V. Müller, D. Maurer, E. W. Scheidt, C. Roth, K. Lüders, E. Bucher, and H. E. Bömmel: Solid State Commun. **57** (1986) 319.

[30] B. S. Shivaram, T. F. Rosenbaum, and D. G. Hinks: Phys. Rev. Lett. **57** (1986) 1259.

[31] B. Ellman, L. Taillefer, and M. Poirier: Phys. Rev. B **54** (1996) 9043.

[32] J. P. Brison, N. Keller, P. Lejay, J. L. Tholence, A. Huxley, N. Bernhoeft, A. I. Buzdin, B. Fåk, J. Flouquet, L. Schmidt, A. Stepanov, R. A. Fisher, N. Phillips, and C. Vettier: J. Low Temp. Phys. **95** (1994) 145.

[33] A. P. Ramirez, N. Stücheli, and E. Bucher: Phys. Rev. Lett. **74** (1995) 1218.

[34] A. Yaouanc, P. D. de Réotier, A. Huxley, J. Flouquet, P. Bonville, P. C. M. Gubbens, and A. M. Mulders: J. Phys.: Condens. Matter **10** (1998) 9791.

[35] Y. Kohori, T. Kohara, H. Shibai, Y. Oda, Y. Kitaoka, and K. Asayama: J. Phys. Soc. Jpn. **57** (1988) 395.

[36] K. Tenya, M. Ikeda, T. Tayama, T. Sakakibara, E. Yamamoto, K. Maezawa, N. Kimura, R. Settai, and Y. Ōnuki: Phys. Rev. Lett. **77** (1996) 3193.

[37] Y. Machida, A. Itoh, Y. So, K. Izawa, Y. Haga, E. Yamamoto, N. Kimura, Y. Onuki, Y. Tsutsumi, and K. Machida: arXiv:1107.3082.

[38] K. A. Park and R. Joynt: Phys. Rev. Lett. **74** (1995) 4734.

[39] R. Joynt: J. Phys.: Condens. Matter **2** (1990) 3415.

[40] D.-C. Chen and A. Garg: Phys. Rev. Lett. **70** (1993) 1689.

[41] M. Ozaki, K. Machida, and T. Ohmi: Prog. Theor. Phys. **75** (1986) 442.

[42] M. Ozaki, K. Machida, and T. Ohmi: Prog. Theor. Phys. **74** (1985) 221.

[43] M. Ozaki and K. Machida: Phys. Rev. B **39** (1989) 4145.

[44] K. Machida, T. Fujita, and T. Ohmi: J. Phys. Soc. Jpn. **62** (1993) 680.

[45] T. Fujita, W. Aoyama, K. Machida, and T. Ohmi: J. Phys. Soc. Jpn. **63** (1994) 247.

[46] Y. Hirano, T. Fujita, K. Machida, and T. Ohmi: J. Phys. Soc. Jpn. **64** (1995) 210.

[47] G. E. Volovik and L. P. Gor'kov: Zh. Eksp. Teor. Fiz. **88** (1985) 1412 [Translation: Sov. Phys. JETP **61** (1985) 843].

[48] P. D. de Réotier, A. Huxley, A. Yaouanc, J. Flouquet, P. Bonville, P. Imbert, P. Pari, P. C. M. Gubbens, and A. M. Mulders: Phys. Lett. A **205** (1995) 239.

[49] G. M. Luke, A. Keren, L. P. Le, W. D. Wu, Y. J. Uemura, D. A. Bonn, L. Taillefer, and J. D. Garrett: Phys. Rev. Lett. **71** (1993) 1466.

[50] A. J. Leggett: Rev. Mod. Phys. **47** (1975) 331.

[51] G. Eilenberger: Z. Phys. **214** (1968) 195.

[52] N. Schopohl: J. Low Temp. Phys. **41** (1980) 409.

[53] J. W. Serene and D. Rainer: Phys. Rep. **101** (1983) 221.

[54] M. Fogelström and J. Kurkijärvi: J. Low Temp. Phys. **98** (1995) 195.

[55] J. A. Sauls and M. Eschrig: New J. Phys. **11** (2009) 075008.

[56] Y. Nagato, K. Nagai, and J. Hara: J. Low Temp. Phys. **93** (1993) 33.

[57] N. Schopohl and K. Maki: Phys. Rev. B **52** (1995) 490.

[58] M. Ichioka, N. Hayashi, and K. Machida: Phys. Rev. B **55** (1997) 6565.

[59] M. Ichioka, A. Hasegawa, and K. Machida: Phys. Rev. B **59** (1999) 8902.

[60] M. Ichioka, A. Hasegawa, and K. Machida: Phys. Rev. B **59** (1999) 184.

[61] J. M. Luttinger and J. C. Ward: Phys. Rev. **118** (1960) 1417.

[62] D. Vollhardt and P. Wölfle: *The Superfluid Phase of Helium 3* (Taylor and Francis, London, 1990).

[63] E. V. Thuneberg: Phys. Rev. Lett. **56** (1986) 359.

[64] E. V. Thuneberg: Phys. Rev. B **36** (1987) 3583.

[65] M. M. Salomaa and G. E. Volovik: Phys. Rev. Lett. **51** (1983) 2040.

[66] M. M. Salomaa and G. E. Volovik: Phys. Rev. B **31** (1985) 203.

[67] G. E. Volovik and V. P. Mineev: Pis'ma Zh. Eksp. Teor. Fiz. **24** (1976) 605 [Translation: JETP Lett. **24** (1976) 561].

[68] A. Huxley, P. Rodiere, D. M. Paul, N. van Dijk, R. Cubitt, and J. Flouquet: Nature **406** (2000) 160.

[69] I. Vekhter, P. J. Hirschfeld, J. P. Carbotte, and E. J. Nicol: Phys. Rev. B **59** (1999) R9023.

[70] P. Miranović, M. Ichioka, K. Machida, and N. Nakai: J. Phys.: Condens. Matter **17** (2005) 7971.

[71] T. Sakakibara, A. Yamada, J. Custers, K. Yano, T. Tayama, H. Aoki, and K. Machida: J. Phys. Soc. Jpn. **76** (2007) 051004.

[72] T. Trappmann, H. v. Löhneysen, and L. Taillefer: Phys. Rev. B **43** (1991) 13714.

[73] P. A. Midgley, S. M. Hayden, L. Taillefer, B. Bogenberger, and H. v. Löhneysen: Phys. Rev. Lett. **70** (1993) 678.

[74] K. Elboussiri: Appl. Phys. A **59** (1994) 223.

[75] B. Ellman, A. Zaluska, and L. Taillefer: Physica B **205** (1995) 346.

[76] B. Ellman, M. Sutton, B. Lussier, R. Brunig, L. Taillefer, and S. Hayden: arXiv:cond-mat/9704125.

[77] M. Sato: private communication.

[78] Y. Tsutsumi, T. Mizushima, M. Ichioka, and K. Machida: J. Phys. Soc. Jpn. **79** (2010) 113601.

[79] Y. Tsutsumi, M. Ichioka, and K. Machida: Phys. Rev. B **83** (2011) 094510.